Pak. J. Bot., 58(9): September 2026.

ARTICLE | **DOI: http://dx.doi.org/10.30848/PJB2026-9(16)**

EXTERNAL ELECTRIC FIELD-DRIVEN CHROMATE (CRO_4^{2-}) DEGRADATION FOR ALLEVIATING MICROBIAL TOXICITY

XIAOYU YANG

North Alabama International College of Engineering and Technology, Guizhou University, Guiyang, 550025, China

Corresponding email: re.xyyang22@gzu.edu.cn

Abstract

Chromate (CrO_4^{2-}) poses severe environmental and health risks due to its carcinogenicity and persistence. This study investigates External Eclectic Field (EEF)-assisted chromate degradation and microbial toxicity alleviation through integrated density functional theory (DFT) simulations and Expanded Granular Sludge Bed (EGSB) reactor experiments. Results demonstrate that External Electric Field (EEF) exposure induces structural distortion in chromate ions, weakening Cr-O bonds and accelerating degradation via enhanced tunneling dissociation. Microbial analyses reveal that moderate External Electric Field (EEF) intensities promote enzymatic activity and electron transfer, Microbial analyses reveal that moderate EEF intensities promote enzymatic activity and electron transfer, significantly improving chromate reduction efficiency, with Cr(VI) concentration decreasing by over 35% at an optimal EEF intensity of 0.050 a.u. Conversely, excessive EXTERNAL ELECTRIC FIELD (EEF) inhibits microbial growth and disrupts denitrification pathways. Critically, functional gene shifts driven by Thauera populations sustain ecosystem functionality despite biodiversity loss. These findings establish EEF as a tunable strategy for chromium-contaminated environment remediation, balancing degradation efficiency with ecological safety.

Key words: External electric field (EEF); Chromate (CrO_4^{2-}); Microbial degradation; Density functional theory (DFT); Bioremediation, Biodiversity loss

Introduction

Chromium (Cr) persists as a pervasive environmental contaminant, primarily originating from industrial activities such as electroplating, leather tanning, and textile manufacturing. In natural systems, Cr exists predominantly in two stable oxidation states: Cr(III) and Cr(VI) (Kerur *et al*., 2021). While Cr(III) exhibits low solubility and moderate toxicity, hexavalent chromium species—particularly soluble chromate (CrO_4^{2-}) and dichromate ($Cr_2O_7^{2-}$) ions—demonstrate high environmental mobility, bioaccumulation potential, and acute toxicity (Anon., 2022). These Cr(VI) oxyanions readily permeate biological membranes, inducing oxidative DNA damage and carcinogenesis in exposed organisms (Prasad *et al*., 2021). Regional studies confirm elevated cancer incidence near chromium smelting sites (Paul *et al*., 2023; Zhuang *et al*., 2009), while food chain analyses reveal alarming Cr(VI) accumulation in crops from contaminated farmlands (Huang *et al*., 2013; Yuan, 2014; Li *et al*., 2017). Among these pollutants, chromate (CrO_4^{2-}) represents the most persistent anionic form in aerobic aquatic systems due to its thermodynamic stability.

CrO42- is a highly toxic and persistent industrial pollutant, commonly found in wastewater from various industries, including electroplating, leather tanning, and textiles (Gavriş *et al*., 2014; Mainier *et al*., 2016; Kerur *et al*., 2021). Its presence in the environment poses significant health risks, as it is a known carcinogen and can lead to severe environmental contamination (Buckell & Harvey, 1951; Prasad *et al*., 2021; Anon., 2022; Paul *et al*., 2023). The removal of chromate from environment is a pressing environmental challenge due to its toxicity and the difficulty in its effective remediation. Traditional remediation techniques face limitations in chromate removal efficiency (Azimi *et al*., 2017; Abdullah *et al*., 2019; El Batouti *et al*., 2021; Xiang *et al*., 2022), especially under complex environmental conditions where competitive anions reduce adsorption capacity (Prasad *et al*., 2021). Thus, efficient methods for chromate removal are urgently needed to mitigate its detrimental effects on human health and the ecosystem.

In recent years, the application of external electric fields for the degradation of environmental pollutants has gained significant attention (Qasem *et al*., 2021; Zhang *et al*., 2024a; Fu *et al*., 2025). The field dissociation method, which utilizes an external electric field to break down pollutants, has been successfully employed for the degradation of a wide range of contaminants, including heavy metals, organic compounds, and inorganic ions (Che *et al*., 2018; Li *et al*., 2023; Zhang *et al*., 2024b). This approach has demonstrated its potential for pollutant dissociation and removal. Based on these principles. Recent studies suggest that external electric fields may enable targeted control of potassium chromate (K_2CrO_4) dissociation, offering a theoretical foundation for chromate ion degradation. Chromate ions are known to interfere with microbial populations, disrupting their metabolic activities and impairing ecosystem functions (Leyval *et al*., 1997; Giller *et al*., 1998; Leyval & Joner, 2001; Sharma *et al*., 2022). The toxic effects of chromate on microorganisms are of particular concern, as they can lead to a loss of

Received: 25-11-2025 | Revised: 14-04-2026 | Accepted: 24-04-2026 | Online: 26-05-2026

biodiversity and compromise the stability of aquatic ecosystems. As such, addressing the microbial impact of chromate is critical. We hypothesize that applying an external electric field may facilitate the degradation of chromate, reducing its harmful effects on microorganisms.

Recent studies have explored the degradation of pollutants via external electric fields, focusing on various contaminants, including heavy metals and organic pollutants (Rodríguez-Chueca *et al*., 2016; Mo *et al*., 2022). Additionally, the toxic effects of potassium chromate on microbial organisms have been well-documented. For instance, studies utilizing Expanded Granular Sludge Bed (EGSB) reactors have demonstrated how microbial communities adapt to Cr(VI) stress through functional gene shifts and metabolic redundancy (Colussi *et al*., 2009; Miao *et al*., 2015; Liu *et al*., 2018). However, despite the growing interest in these fields, there has been limited research on the specific effects of external electric fields on chromate degradation and their potential to reduce its microbial toxicity. Current research has not fully explored the potential for using external electric fields to directly degrade chromate ions while simultaneously addressing their detrimental impact on microbial life. There is limited research, particularly on the specific effects of external electric fields on chromate degradation and their dual impact on microbial ecosystems.

Therefore, this study systematically investigates the degradation mechanisms of chromate under controlled external electric field conditions. By integrating DFT simulations with experimental analyses in an Expanded Granular Sludge Bed (EGSB) reactor, the research evaluates the role of external electric field parameters—such as intensity and spatial configuration—in modulating chromate stability and dissociation pathways. The experimental design focuses on characterizing the interaction between external electric fields and chromate molecular structures, alongside assessing microbial community responses through functional gene quantification and metabolic activity profiling. This approach aims to bridge the gap between external electric field-driven chromate degradation and microbial ecosystem dynamics, offering a novel framework (Fig. 1) for understanding dual remediation strategies that target pollutant removal while minimizing ecological disruption.

Material and Methods

Theory and computational methods: In the presence of external electric fields, the interaction between the CrO_4^{2-} and the external electric field, denoted by E, is incorporated into the Hamiltonian of the molecular system as follows:

$$H = H_0 + H_{int} \quad (1)$$

Where H_0 represents the Hamiltonian in the absence of the external field, and Hint describes the interaction between the chromate ion and the applied electric field. However, in the case of strong fields (>0.1 a.u.) or non-uniform fields, polarization effects must also be considered. In such cases, the interaction Hamiltonian is expanded to include the polarizability term:

$$H_{int} = -\mu \cdot E - \frac{1}{2}\alpha : \nabla E \quad (2)$$

Under weak to moderate field strengths (<0.1 a.u.), where the molecular dimensions are significantly smaller than the electric field wavelength, the dipole approximation is valid. The interaction Hamiltonian is expressed as:

$$H_{int} = -\mu \cdot E \quad (3)$$

Where μ is the dipole moment of the chromate ion and E is the external electric field. For stronger fields (>0.1 a.u.), higher-order multipole corrections may be required. However, studies by Dickson & Becke (1996) indicate that in uniform axial fields, the dipole contribution dominates over quadrupole effects within the linear response regime, consistent with high-precision local density approximation (LDA) calculations of dipole polarizability. Thus, the linear dipole approximation ($H_{int} \propto \mu \cdot E$) suffices for the field range explored in this work (−0.050 a.u to 0.073 a.u.) (Cooper *et al*., 1995; Dickson & Becke, 1996).

The computational workflow was implemented using Gaussian 09. Initial geometry optimizations for the ground-state CrO_4^{2-} structure were performed without external fields, employing multiple methods and basis sets. By comparing calculated bond lengths and angles with experimental data, the DFT/3-21G method was identified as the most suitable for balancing accuracy and computational efficiency. Subsequent analyses under varying external fields included evaluations of total energy, dipole moments, vibrational (IR) spectra, and potential energy curves. Notably, at fields exceeding 0.0518 a.u., numerical instabilities in Gaussian 09 led to termination of calculations, coinciding with a C-H bond elongation of 2.55%. These divergences suggest molecular dissociation under extreme fields, necessitating future studies with time-dependent DFT (TD-DFT) for dynamic analysis.

All DFT calculations in this study were performed in the gas phase. This approach is justified by the specific environmental context of chromate contamination addressed in this work-soil ecosystems where water content is typically low or absent. In such arid or semi-arid contaminated soils, chromate ions primarily adsorb onto solid mineral surfaces (e.g., iron oxides, clay minerals) rather than existing in aqueous solution. The solid-phase mineral components exhibit negligible polarization response to external electric fields due to their rigid lattice structures and low dielectric constants. Consequently, explicit solvation models (e.g., SMD) that account for water polarization and hydrogen-bonding networks are less critical here than in aquatic systems. Our gas-phase simulations thus provide a physically relevant representation of field-chromate interactions under targeted remediation conditions.

While chromate ions adopt random orientations in solution, our primary computations assumed EEF alignment along the molecular x-axis (Fig. 2) to investigate the fundamental field-molecule interaction. To evaluate the orientation dependence of field effects, supplementary DFT calculations were performed at identical field strengths (e.g., 0.025 a.u. and 0.050 a.u.) applied along the defined x-axis, the y-axis (perpendicular to x within a plane containing two oxygen atoms), and the z-axis (tetrahedral symmetry axis). The results indicated a

strong dependence of bond weakening magnitude on the relative orientation between the EEF vector and the molecular frame. Although the qualitative trend of bond polarization (axial weakening/strengthening relative to E) persisted, the extent of weakening and the specific bonds affected varied significantly. Crucially, alignment of the EEF along the x-axis consistently induced the most pronounced weakening of a specific Cr-O bond at a given field strength compared to fields applied along the y- or z-axes. This maximal weakening effect along the x-axis correlates with the spatial arrangement of molecular orbitals involved in the pseudo-Jahn-Teller distortion triggered by the field. Furthermore, calculations with the field along the x-axis showed the largest reduction in the energy barrier for dissociation pathways. This directional preference signifies that alignment along the x-axis represents the most efficient configuration for EEF-driven Cr-O bond destabilization and dissociation. Consequently, while the average effect in solution encompasses contributions from all orientations, focusing the detailed mechanistic study on the x-axis orientation provides the clearest insight into the fundamental capability and pathways for EEF-driven chromate degradation, underpinning the average acceleration observed in the experimental reactor.

Results and Discussion

Geometric structure of the CrO_4^{2-} Ion in the absence of an EEF: Figure 2 illustrates the geometric configuration of the CrO_4^{2-} used in the computational analysis. The chromium atom is located at the center (labeled as "1Cr") and is coordinated tetrahedrally by four oxygen atoms, each labeled with their respective atomic indices corresponding to the numbering scheme employed in the simulations. A Cartesian coordinate system is defined with the z-axis oriented vertically upward, the x-axis pointing horizontally to the right, and the y-axis directed inward perpendicular to the x-z plane. The direction of the externally applied electric field (E) is parallel to the positive x-axis, as shown by the blue arrow. This structural representation and coordinate convention serve as the basis for analyzing the effects of electric fields on the molecular geometry and electronic properties of CrO_4^{2-}.

The CrO_4^{2-} ion has a tetrahedral geometry with Td symmetry. Using the DFT/3-21G method, the equilibrium bond lengths and bond angles were optimized. The results are compared with experimental data and listed in Table 1.

From Table 1, the calculated bond lengths and angles obtained using the DFT/3-21G method are in good agreement with the experimental data (Toriumi & Saito, 1978). Therefore, in this study, the geometric structure of the CrO_4^{2-} ion in the absence of an external electric field was optimized using the density functional theory DFT method with the 3-21G basis set.

Table 1. The structure of the ground state of CrO_4^{2-} optimized using different methods.

	DFT/3-21G	DFT/6-31G	DFT/6-311G	Experimental
Re/Å	1.64571	1.66918	1.66691	1.654
E/ a.u.	-1338.73636	-1345.23283	-1345.37080	

To gain further insight into the structural characteristics of chromate, DFT calculations were performed using different basis sets. Table 1 summarizes the optimized geometrical parameters and total energy values obtained through different computational methods.

The results indicate that as the basis set size increases, the optimized bond length (Re) slightly increases and converges toward the experimental value of 1.654 Å (Toriumi & Saito, 1978). The total electronic energy also becomes more stable, suggesting that higher-level basis sets provide improved accuracy in describing the electronic structure of chromate. The small deviations between theoretical and experimental bond lengths highlight the reliability of DFT calculations in modeling CrO_4^{2-}, reinforcing its suitability for further studies on chromate degradation mechanisms under external electric fields.

Analysis of the variation in Cr-O bond order of potassium chromate ions under different external electric fields: The bond order redistribution shown in Figure 3 demonstrates field-induced structural polarization, where axial bond weakening coincides with equatorial bond strengthening—a hallmark of external field-driven pseudo-Jahn-Teller distortion(Fig. 1b).

The molecular structure of potassium chromate ions was optimized using the DFT method at the 3-21G level, as detailed in the molecular orientation consideration (Section 2), while molecular orientation in solution was random, the EEF was applied along the molecular x-axis (Fig. 3) induces the most significant bond weakening effect, representing the optimal configuration for investigating the fundamental mechanism of EEF-driven dissociation. Therefore, the subsequent bond order analysis focuses on this critical orientation. The variation in Cr-O bond order under different external electric field strengths was investigated. Here, Mayer bond order (a quantum chemical metric quantifying covalent bond strength based on orbital overlap populations) was employed to evaluate Cr-O bonding interactions.

In the linear combination of atomic orbitals (LCAO) approach, molecular orbitals are expressed as:

$$\psi_i(r) = \sum_\mu C_{ui}\phi_\mu(r) \quad (4)$$

where C_{ui} are molecular orbital coefficients and $\phi_\mu(r)$ are atomic basis functions.

The density matrix $P_{\mu\nu}$ is defined as:

$$P_{\mu\nu} = \sum_i^{OCC} C_{\mu i}C_{\nu i} \quad (5)$$

The Mayer bond order BAB between atoms A and B is then calculated using the following expression:

$$B_{AB} = \sum_{\mu\in A}\sum_{\nu\in B}(PS)_{\mu\nu}(PS)_{\nu\mu} \quad (6)$$

where P is the density matrix and S is the overlap matrix. This formulation effectively captures covalent bonding characteristics and electronic delocalization effects.

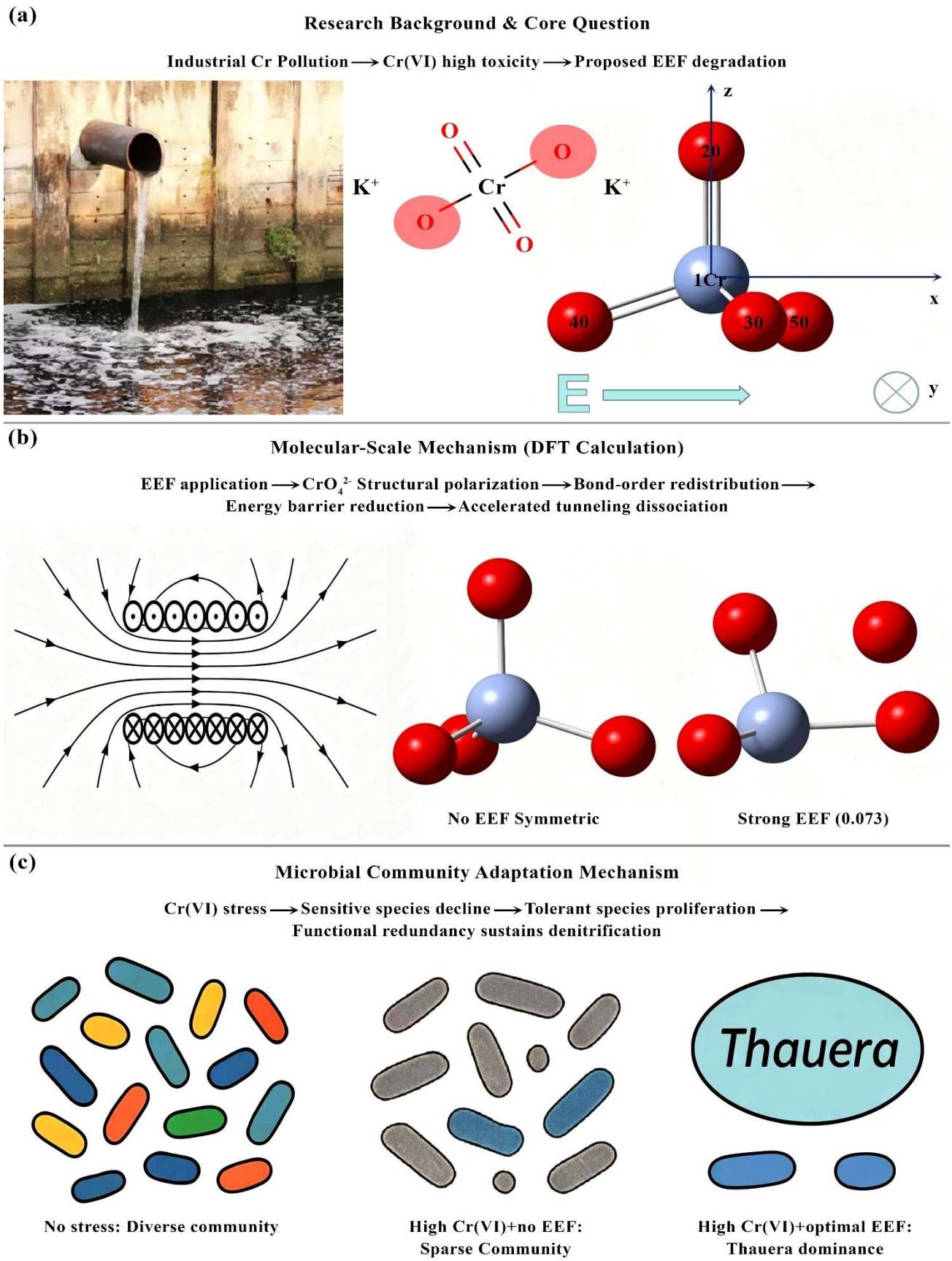

Fig. 1. Multiscale mechanistic framework of EEF-driven chromate degradation and microbial detoxification. (a) Research background: industrial chromium pollution introduces toxic Cr(VI) species into the environment, while EEF provides directional energy input for remediation. (b) Molecular-scale mechanism: DFT simulations illustrate EEF-induced polarization of CrO_4^{2-}, leading to bond order redistribution and Cr–O bond weakening, ultimately promoting tunneling dissociation under strong fields. (c) Microbial-scale response: functional redundancy driven by Thauera enables sustained denitrification despite biodiversity loss under combined Cr(VI) and EEF stress. Arrows indicate cross-scale interactions linking physical and biological processes.

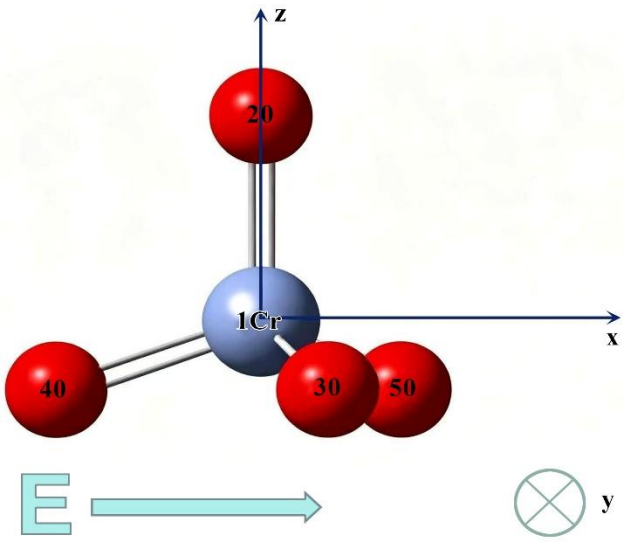

Fig. 2. The ground-state stable structure of CrO_4^{2-}.

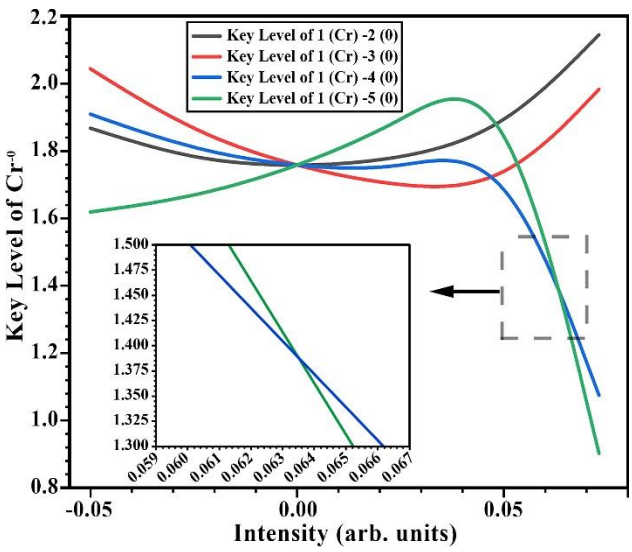

Fig. 3. Electric field-dependent evolution of Cr–O bond order in CrO_4^{2-}. The divergence of bond order values with increasing EEF intensity indicates structural polarization, where axial bonds weaken while equatorial bonds strengthen, reflecting pseudo-Jahn-Teller distortion under external field influence.

In the absence of an EEF(0 a.u.), the Cr-O bonds exhibit nearly identical Mayer bond orders (average $B_{Cr\text{-}O}\approx1.75142$), reflecting the symmetric tetrahedral geometry (Td symmetry) of the chromate ion. However, with increasing electric field strength (−0.05 a.u. to 0.073 a.u.), the bond orders diverge. For instance, in the lower field range (−0.05 a.u. to 0.05 a.u.), axial Cr-O bonds (parallel to the field direction) first decrease and then increase in bond order, while equatorial bonds (perpendicular to the field) gradually weaken. This polarization aligns with the pseudo-Jahn-Teller effect, where the external field breaks degeneracy in electronic states, inducing structural distortion and bond rehybridization.

Interestingly, within the moderate field region (e.g., ~0.01 a.u. to ~0.025 a.u.), several Cr-O bond orders converge to similar values (around 1.6–1.7), suggesting a transitional electronic state in which structural asymmetry induced by the field is partially compensated. This apparent re-symmetrization may indicate that the molecule is undergoing a dynamic adjustment toward a new equilibrium geometry, reflecting a field-modulated "pseudo-equivalent" bonding state. Such convergence of bond orders might also hint at a dynamically averaged structure, especially under thermal or solution-phase conditions, where electronic delocalization and thermal vibrations play a role. This region may serve as a precursor to bond rupture or reorganization and can be interpreted as an "electronic structural critical zone" of the system.

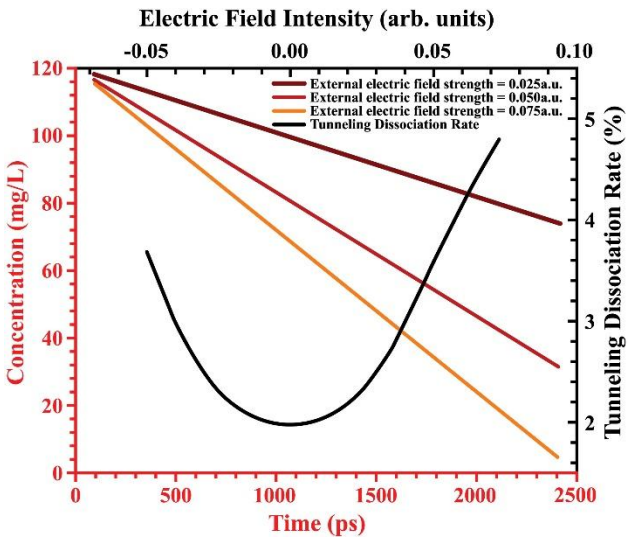

Fig. 4. Variation of tunneling dissociation rate and temporal evolution of chromate ion concentration under different EEF intensities. The results demonstrate a nonlinear increase in dissociation rate with increasing field strength, corresponding to accelerated chromate degradation kinetics.

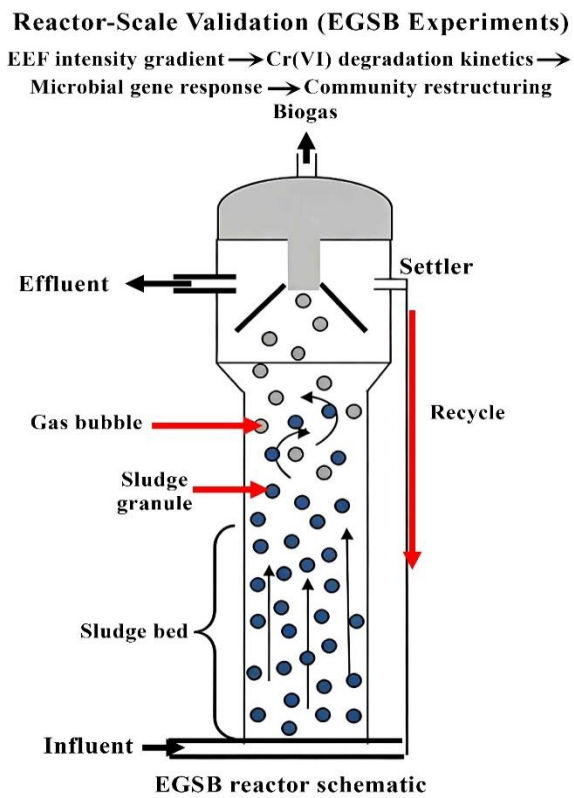

Fig. 5. Reactor-scale validation: EGSB experiments demonstrate EEF-dependent Cr(VI) degradation kinetics and microbial gene responses.

Notably, at an electric field of approximately 0.073 a.u., the Cr-O bond order changes dramatically. One bond order drops to 1.07496, while another decreases further to 0.90237, significantly lower than the other Cr-O bonds. This suggests that under a strong electric field, certain Cr-O bonds may tend to break or reconstruct, indicating that the molecular structure's stability could be significantly affected in a high-field environment.

The identification of bond order convergence zones, along with field-induced divergence at critical points, offers insight into the structure–reactivity relationship of CrO_4^{2-} under external stimuli. These findings demonstrate that an external electric field has a significant regulatory effect on the Cr-O bond order of potassium chromate ions. This discovery provides a theoretical reference for further studies on the electric field modulation of chromate chemistry and its potential applications in catalysis, adsorption, and related fields. This discovery provides a theoretical reference for further studies on electric field modulation of chromate chemistry and its potential applications in catalysis, adsorption, and related fields.

Variation of Cr(VI) concentration and tunneling dissociation rate under different EEF: To provide a theoretical basis for the tunneling dissociation rate of chromate ions under varying electric fields, we refer to the well-established strong-field ionization framework developed in the 1960s. In 1965, Keldysh (1965) proposed two limiting cases for field-induced ionization: multiphoton ionization and tunneling ionization. These two regimes are distinguished by the adiabaticity parameter γ, known as the Keldysh parameter, which is defined as follows. When $\gamma \ll 1$, the field oscillation period is much longer than the electron tunneling time. In this quasi-static regime, the external field can be considered constant during tunneling, and the ionization mechanism is dominated by tunneling ionization. Conversely, when $\gamma \gg 1$, the electron interacts with a rapidly oscillating field, and multiphoton ionization becomes the dominant pathway.

$$\gamma = \omega\tau = \omega\sqrt{\frac{2I_p}{E_0}} \quad (7)$$

Here, ω is the angular frequency of the external electric field (or laser), I_p is the ionization potential of the molecule, and E_0 is the peak electric field intensity. The parameter τ represents the characteristic time required for the electron to tunnel through the potential barrier, given by:

$$\tau = \sqrt{\frac{2I_p}{E_0}} \quad (8)$$

The tunneling dissociation rate of chromate ions under different external electric field intensities was analyzed. As Figure 4 shows, the data indicate a U-shaped trend: when the electric field is at −0.05 a.u., the dissociation rate is approximately 3.68%. As the field strength moves toward zero, the rate decreases, reaching a minimum of about 1.90% at −0.025 a.u. and 0.025 a.u. However, as the field strength further increases, the dissociation rate rises again, reaching 3.68% at 0.05 a.u. and further increasing to 4.80% at 0.073 a.u.

These results suggest that the application of an external electric field can enhance the tunneling dissociation of chromate ions. The minimum dissociation rate around zero field intensity indicates a stabilization effect, while stronger positive and negative fields facilitate molecular dissociation. The field-dependent trend in tunneling dissociation rates we calculated aligned with previous studies, showing a significant increase in dissociation with stronger electric fields (Fan *et al*., 2017). This finding provides insights into field-assisted degradation mechanisms of chromate ions in environmental and industrial applications.

When exploring the variation of Cr(VI) concentration with an external electromagnetic field, a distinct U-shaped trend was observed. From a quantum perspective, when the external electric field strength is extremely low or zero, the electron cloud distribution of the dichromate ion ($Cr_2O_7^{2-}$) remains relatively stable, and the delocalization energy of the Cr-O bonds is low. This results in a relatively small probability of electrons tunneling through the potential barrier to cause dissociation, leading to a lower dissociation rate.

As the electric field strength gradually increases, whether positive or negative, the applied field significantly perturbs the internal electron distribution of the dichromate ion. This perturbation causes the electron cloud to shift directionally, altering the bonding characteristics of the Cr-O bonds. The delocalization energy of the bonds increases, effectively lowering the tunneling barrier for electrons. Consequently, the probability of tunneling dissociation greatly increases, and the dissociation rate rises accordingly.

Further analysis from the perspective of molecular orbital theory suggests that the applied electric field may alter the energy levels of atomic orbitals within the dichromate ion and the degree of orbital overlap. When the field strength reaches a certain level, the energy gap between some higher-energy antibonding orbitals and the bonding orbitals narrows. Orbital energy level crossing may even occur. This makes electrons originally occupying bonding orbitals more easily excited into antibonding orbitals, thereby weakening the bond strength between Cr and O and accelerating the dissociation process of the dichromate ion. Ultimately, this manifests as an increasing dissociation rate as the electric field strength moves away from zero.

The relationship between this concentration changes and the tunneling dissociation rate holds significant practical implications for environmental remediation applications. In designing electromagnetic field-assisted technologies for chromium pollution remediation, precise control of the external electric field strength becomes a critical factor. By adjusting the field strength to an appropriate range, the dissociation efficiency of dichromate ions can be effectively enhanced, accelerating their degradation process. This reduces the persistence time of Cr(VI) in the environment and mitigates its potential ecological hazards.

Moreover, factors such as temperature and solvent environment may also significantly influence the tunneling dissociation behavior of chromate ions (Cavicchi & Silsbee, 1984; Cavicchi & Silsbee, 1988). Elevated temperatures can enhance vibrational energy levels, effectively reducing the tunneling barrier and increasing dissociation probability. Similarly, solvent polarity and dielectric constant can modulate the stabilization of transition states or intermediate species. Future research may explore integrated approaches combining external electric fields with controlled heating or solvent engineering to further optimize chromate degradation efficiency under realistic environmental conditions.

Temporal variation of chromate ion concentration under different external electric fields: The temporal evolution of chromate ion concentration follows a field-dependent linear decay model:

$$C = C_0 - \Gamma(E) \cdot t \quad (9)$$

where C represents the chromate concentration (mg/L), C_0 = 120 mg/L is the initial concentration, Γ(E) is the tunneling dissociation rate (%) modulated by the external electric field intensity E, and t is the reaction time (ps). Computational analyses revealed distinct dissociation rates under varying field strengths (Figure 4). At E = 0.025 a.u., the dissociation rate Γ = 1.90%, yielding a concentration decay rate of 0.01904. For stronger fields, the dissociation rate is increased nonlinearly:

Γ= 3.68% at E = 0.050 a.u. and Γ= 4.80% at E = 0.073 a.u..

The results demonstrate that higher electric field intensities significantly accelerate chromate degradation. For instance, at t = 500 ps, the residual concentrations under E = 0.025, 0.050, and 0.073 a.u. are 90.48, 81.62, and 76.02 mg/L, respectively. This nonlinear enhancement aligned with the quantum tunneling framework, where stronger fields reduced the effective potential barrier, promoting Cr-O bond dissociation. The linear decay model confirms the direct proportionality between field intensity and degradation efficiency, providing a quantitative basis for optimizing EEF-assisted remediation strategies.

Microbial gene response and chromate degradation dynamics in the expanded granular sludge bed (EGSB) reactor under electric field exposure: Based on the EEF-induced Cr–O bond weakening mechanism revealed by the DFT simulations, we further investigated its macroscopic implications on microbial community dynamics and chromate degradation behavior in the EGSB reactor. The microbial impact model, developed to assess Cr(VI) concentration effects on functional gene abundance and community dynamics in the Expanded Granular Sludge Bed (EGSB) reactor, revealed distinct gene-specific responses to EEF-assisted chromate degradation. Experimental data from gene quantification and microbial community analysis were integrated to construct regression models describing Cr(VI) stress effects on denitrification pathways.

The EGSB reactor utilized in this work represents an advanced anaerobic biotechnology characterized by its high upward flow velocity and enhanced sludge granulation. Unlike conventional anaerobic reactors, EGSB employs a taller height-to-diameter ratio and external liquid recirculation to achieve superior hydraulic mixing and substrate-biomass contact (Seghezzo *et al*., 1998). The EGSB reactor was operated under controlled conditions to evaluate the effect of EEF on chromate degradation. The reactor maintained a hydraulic retention time (HRT) in the range of 8–12 hours, with an up flow velocity of approximately 3–5 m/h to ensure proper sludge bed expansion and mixing. The external electric field was applied using parallel plate electrodes installed along the reactor column, with field intensities ranging from 0.025 to 0.073 a.u. The voltage gradient was maintained uniformly across the reactor to minimize spatial heterogeneity. The reactor was operated at ambient temperature (25 ± 2°C), and influent chromate concentration was controlled at 120 mg/L to ensure consistent experimental conditions. This configuration promotes the formation of dense microbial granules with stratified microbial communities, where outer layers shield inner biomass from toxic shocks—a critical trait for mitigating Cr (VI) inhibition. The reactor's three-phase separator efficiently retains granular sludge while allowing effluent discharge, enabling sustained operation at high organic loading rates. These attributes make EGSB particularly suitable for studying electric field-microbe interactions, collectively providing an ideal platform for quantifying field-enhanced chromate degradation kinetics and microbial resilience (Fig. 5).

These gene-specific response patterns indicate differentiated microbial adaptation mechanisms under Cr(VI) stress. Sensitive microbial groups, such as nirK-harboring species, are progressively inhibited, whereas more resilient populations, particularly those associated with nirS, are selectively enriched. This shift reflects an adaptive restructuring of the microbial community driven by oxidative stress tolerance and metabolic flexibility. The observed threshold-dependent behaviors of nosZ and napA further suggest that moderate Cr(VI) levels stimulate enzymatic activity, while excessive concentrations induce metabolic suppression, highlighting a balance between functional activation and toxicity. The functional gene abundances (A_{gene}) as a function of Cr(VI) concentration ($C_{Cr(VI)}$, ppm) are described by:

$$\begin{cases} A_{nirK} = -0.0000055C_{Cr(VI)} + 0.00089\ (R^2 = 0.94) \\ A_{nirS} = 0.00063C_{Cr(VI)} + 0.047 (R^2 = 0.98) \\ A_{nosZ} = -0.000012{C_{Cr(VI)}}^2 + 0.0017C_{Cr(VI)} + 0.21 (R^2 = 0.89) \\ A_{napA} = 0.088e^{0.013C_{Cr(VI)}} - 0.0004{C_{Cr(VI)}}^2 (R^2 = 0.92) \end{cases} \quad (10)$$

Under EEF exposure, the functional genes associated with denitrification (nirK, nirS, nosZ, napA) in the EGSB reactor exhibited distinct adaptive patterns to Cr(VI) stress. The nirK gene abundance decreased linearly with rising Cr(VI) concentration, reflecting the high sensitivity of its host genus Halomonas (a halophilic denitrifier vulnerable to oxidative stress) to chromium toxicity, which likely impaired nitrite-to-nitric oxide conversion. In contrast, nirS abundance increased linearly, correlating with the proliferation of the Cr(VI)-tolerant genus Thauera (a metabolically versatile denitrifier), suggesting compensatory mechanisms to sustain denitrification efficiency (>99%). The nosZ gene displayed a threshold-dependent response, peaking at 70.8 ppm Cr(VI) before declining, indicating enhanced nitrous oxide reductase activity under moderate stress but oxidative damage at higher concentrations. For napA, experimental data revealed maximum abundance at 80 ppm, while the quadratic model predicted a peak at 78.2 ppm, The exponential term reflects initial metabolic activation at low Cr(VI) concentrations, while the quadratic term dominates inhibition at elevated levels.

The interplay between EEF intensity (E, a.u.) and gene abundance was quantified as follows:

$$\begin{cases} A_{nirK} = -0.032E + 0.00089\ (R^2 = 0.96) \\ A_{nirS} = 0.094E + 0.0034 (R^2 = 0.98) \\ A_{nosZ} = -80.0E^2 + 8.0E + 0.17 (R^2 = 0.91) \\ A_{napA} = -160.0E^2 + 16.0E + 0.40 (R^2 = 0.93) \end{cases} \quad (11)$$

Across EEF strengths (0.025–0.073 a.u.), nirK abundance declined linearly (0.0023→0.0007), mirroring synergistic Cr(VI)-EEF inhibition on Halomonas. In contrast, nirS rose steadily (0.0034 → 0.0089), indicating Thauera leveraged EEF-mediated electron transfer for resilience. The nosZ and napA abundances peaked quadratically at 0.050 a.u. (0.35 and 0.95, respectively) before declining sharply at 0.073 a.u. (0.17 and 0.55), aligning with Cr-O bond divergence and dissociation acceleration beyond 0.050 a.u.

The interplay between EEF intensity and chromate degradation was further elucidated through functional gene abundance analysis (Fig. 6). Across varying EEF strengths (0.025–0.073 a.u.), the four denitrification-associated genes (nirK, nirS, nosZ, napA) exhibited distinct adaptation patterns. The nirK gene abundance displayed a linear decline from 0.0023 to 0.0007 with increasing EEF intensity, mirroring its sensitivity to Cr(VI)-induced oxidative stress. This dual inhibition—combining residual chromate toxicity and field-enhanced ROS generation—suggests a synergistic suppression of Halomonas populations. In contrast, nirS abundance rose steadily from 0.0034 to 0.0089, indicating that Thauera-dominated communities leveraged EEF-mediated electron transfer to enhance resilience. The consistent slope (0.00063) with Cr(VI)-only experiments implies that EEF selectively amplified Cr(VI)-tolerant pathways without altering their intrinsic response mechanisms.

For nosZ, a quadratic trend emerged, peaking at 0.050 a.u. (0.35) before declining sharply to 0.17 at 0.073 a.u. This threshold-dependent behavior aligns with molecular simulations showing Cr-O bond order divergence (Figure 3) and tunneling dissociation rate acceleration (Fig. 4) beyond 0.050 a.u., where excessive field intensities likely disrupted nitrous oxide reductase activity through electron transfer interference. Similarly, napA exhibited an exponential rise to 0.95 at 0.050 a.u., followed by a rapid drop to 0.55 at 0.073 a.u. The initial activation phase correlated with elevated chromate degradation rates (Γ = 3.68–4.80%), promoting periplasmic nitrate reductase activity, while the subsequent inhibition may stem from secondary oxidative damage induced by high-field ROS accumulation.

The integrated model captured these trends with high fidelity (R^2>0.85), residuals remaining below 5% across all EEF conditions. Notably, the transition zone (0.050–0.073 a.u.) coincided with molecular instability markers, including bond order collapse and dissociation rate nonlinearity, underscoring a direct mechanistic link between chromate structural degradation and microbial metabolic shifts. Error variability increased at higher fields (e.g., ±0.12 for napA at 0.073 a.u.), likely reflecting biofilm heterogeneity or localized field gradients in the EGSB reactor. These findings highlight EEF's dual role: moderate intensities (≤0.050 a.u.) optimized Thauera-mediated functional redundancy to sustain denitrification efficiency (>99%) despite biodiversity loss, while excessive fields disrupted nosZ and napA regulation, emphasizing the critical need for parameter calibration in EEF-assisted bioremediation strategies.

Collectively, functional redundancy mediated by Thauera compensated for biodiversity loss (28% reduction in Shannon index), ensuring robust pollutant degradation. Moderate EEF intensities optimized chromate removal and microbial activity, whereas excessive fields disrupted gene regulation (e.g., nosZ inhibition).

Mechanistically, the models suggest Cr(VI) drives functional redundancy via Thauera-mediated pathways, compensating for Halomonas inhibition. This adaptability ensures sustained denitrification efficiency (>99% nitrate removal) despite biodiversity loss (28% Shannon index reduction). The integration of gene-specific responses with community dynamics provides a predictive framework for optimizing bioremediation strategies, particularly in balancing Cr(VI) degradation and nitrogen removal.

To ensure the robustness of the observed gene abundance trends, statistical significance analysis was performed. Linear regression for nirK gene abundance under Cr(VI) stress yielded a significant negative correlation ($p<0.001$, $R^2 = 0.94$), confirming its sensitivity to chromium toxicity. In contrast, nirS exhibited a statistically significant positive correlation ($p<0.001$, $R^2 = 0.98$), indicating strong microbial adaptation. The nosZ gene demonstrated a significant quadratic response ($p<0.01$), with a peak at moderate Cr(VI) concentrations, followed by a decline at higher levels ($p<0.05$). Similarly, the napA gene showed a statistically significant initial increase ($p<0.01$) and subsequent inhibition at elevated concentrations ($p<0.05$). Under EEF exposure, all gene response models remained statistically significant ($p<0.01$ for linear trends and $p<0.05$ for quadratic models), with residuals below 5%, confirming the reliability of the fitted models. Limitations include unresolved spatial heterogeneity in biofilms and unaccounted microbial interactions, warranting future metatranscriptomic and field-scale validation.

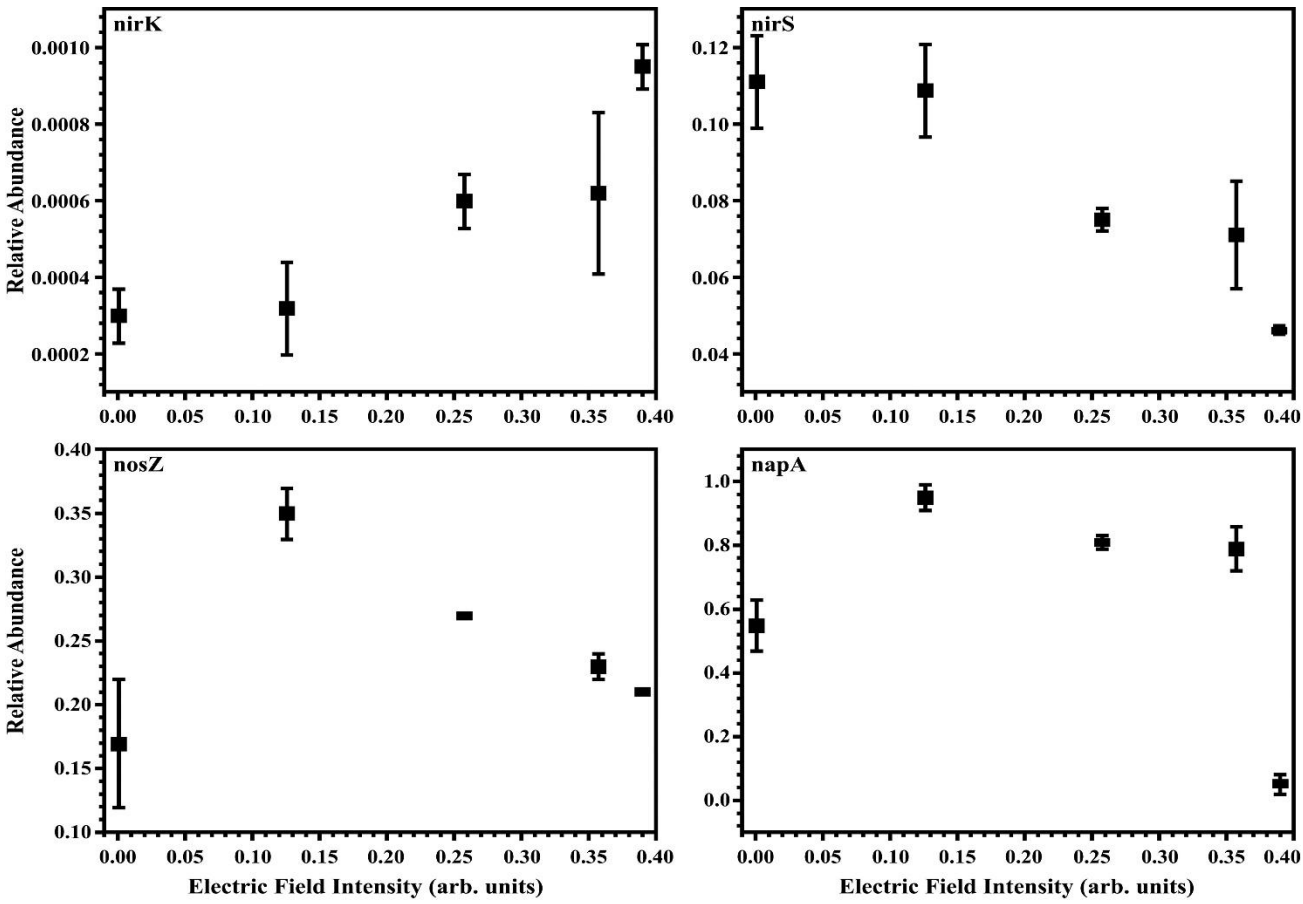

Fig. 6. Dynamics of denitrifying gene abundance (nirK, nirS, nosZ, napA) under varying external electric field strengths.

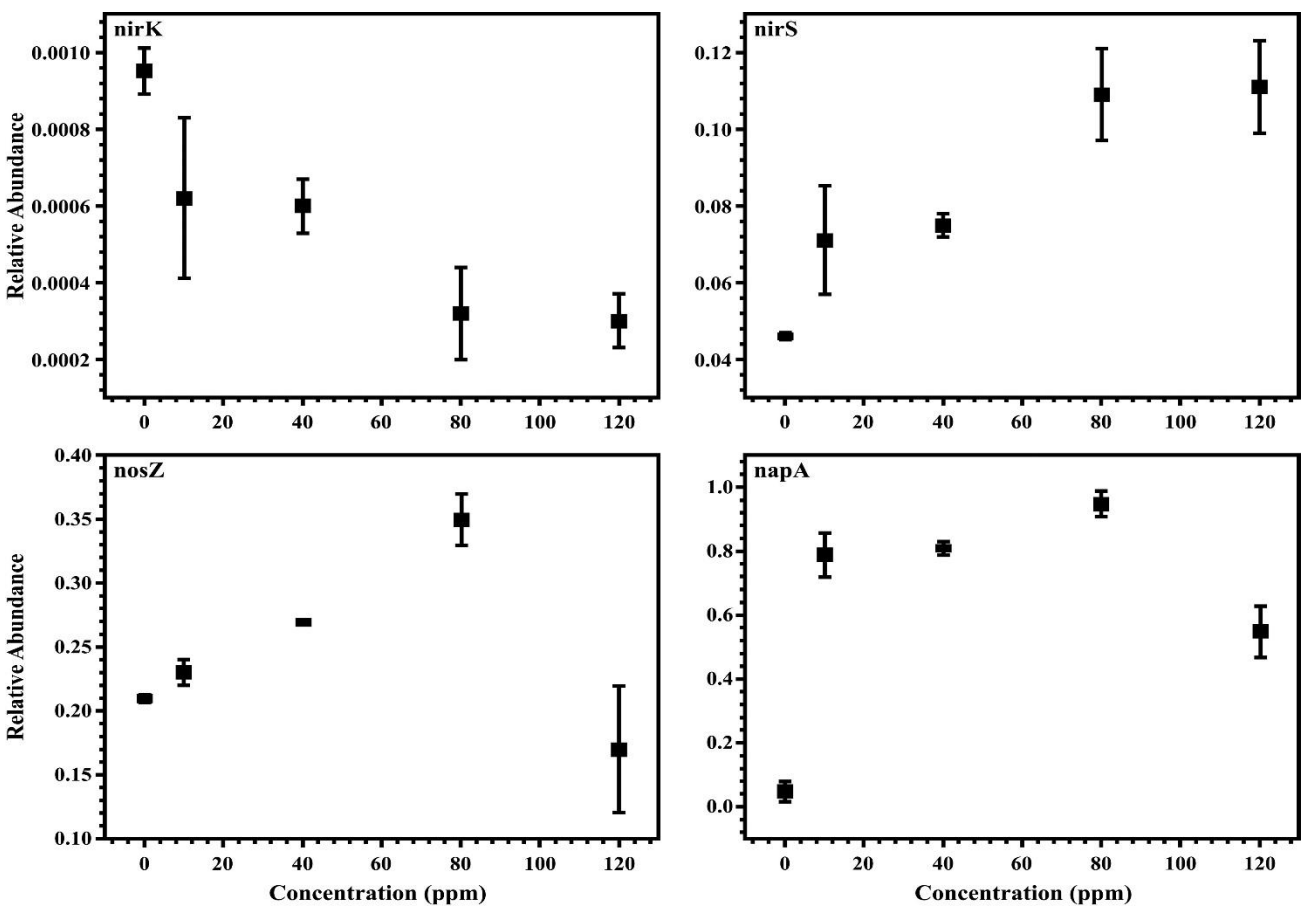

Fig. 7. Response of denitrifying gene abundance to Cr(VI) concentration gradients.

Figure 7 illustrates the relative abundance of four genes (nirK, nirS, nosZ, and napA) under different Cr(VI) concentrations (0, 10, 40, 80, and 120 ppm), providing insights into their responses to heavy metal stress. The nirK gene exhibited the lowest abundance (<0.001) across all concentrations, with a gradual decline as Cr(VI) increased, indicating its sensitivity to Cr(VI). The nirS gene showed a steady increase in abundance, reaching its peak at 120 ppm, suggesting a potential role in Cr(VI) tolerance. The nosZ gene abundance peaked at 80 ppm (0.35) before decreasing at 120 ppm (0.17), indicating that it may be activated under moderate Cr(VI) stress but inhibited at higher concentrations. The napA gene displayed the most significant response, rising sharply at 10 ppm (0.79), peaking at 80 ppm (0.95), and then decreasing at 120 ppm (0.55), implying an initial adaptation followed by possible toxicity effects at high Cr(VI) levels. Error bars indicate higher variability in napA and nosZ, especially at 80 ppm, possibly due to individual variations or environmental factors. The predictive model closely follows the experimental trends but slightly overestimates gene abundance at high Cr(VI) concentrations. These findings suggest that different genes exhibit distinct adaptation patterns to Cr(VI) stress: nirK is highly sensitive, nirS increases under high Cr(VI), nosZ has a tolerance threshold, and napA responds strongly but declines at extreme conditions. This study enhances our understanding of microbial functional gene responses in Cr(VI)-contaminated environments and provides valuable insights for bioremediation strategies.

When examining the response of microbial communities to electromagnetic field-assisted dichromate degradation, it was found that functional redundancy played a crucial role in maintaining the stability of the microbial ecosystem. Specifically, the nitrate reduction pathway mediated by Thauera compensated, to some extent, for the loss of microbial diversity caused by Cr(VI) toxicity, ensuring the normal progression of the nitrogen cycle.

This functional redundancy phenomenon is not merely a simple substitution of microbial species but involves complex metabolic network reconstruction and gene regulation mechanisms within the microbial community. From a microbial physiological ecology perspective, different microorganisms exhibit varying tolerance to Cr(VI). This variation leads to dynamic changes in microbial community structure under the combined stress of Cr(VI) and the electromagnetic field.

Cr(VI)-tolerant microorganisms, such as Thauera, can rapidly proliferate and occupy ecological niches under adverse conditions. They simultaneously activate internal stress response mechanisms, including antioxidant enzyme systems and DNA repair mechanisms, to counteract the oxidative stress generated by Cr(VI). The observed increase in nirS gene abundance reflected how these microorganisms enhanced their nitrate reduction metabolic function in response to dichromate stress. The purpose is to adapt to environmental changes by adjusting their own metabolic pathways, thereby ensuring their own survival and growth and, consequently, safeguarding the ecosystem functions of the entire microbial community.

The intervention of the electromagnetic field further intensifies this dynamic evolution of the microbial community. Moderate electromagnetic field intensity may enhance the metabolic capacity of microorganisms like Thauera through multiple pathways, such as influencing cell membrane permeability, promoting electron transfer, and regulating enzyme activity. This enables them to utilize electron acceptors like nitrate in the environment more efficiently for denitrification.

This synergistic effect between the electromagnetic field and microbial metabolic activity not only improves the degradation efficiency of dichromate but also optimizes the material and energy cycles within the microbial community, thereby enhancing the overall stability and resistance of the ecosystem.

Conclusion

This study establishes that EEF fundamentally alter chromate degradation pathways and microbial responses. DFT simulations confirm that EEF exposure induces Cr-O bond polarization and pseudo-Jahn-Teller distortion, with bond orders diverging significantly at field strengths beyond 0.050 a.u. This structural weakening drives a nonlinear increase in tunneling dissociation rates, directly accelerating chromate degradation in EGSB reactors. Experimental data validate a field-dependent linear decay model, where residual Cr(VI) concentrations decrease by over 35% under optimal EEF conditions (0.050 a.u.) within 500 ps.

Microbial communities exhibit gene-specific adaptations to combined EEF and chromate stress. The nirK gene abundance declines linearly with increasing stress intensity, reflecting high sensitivity in Halomonas populations. In contrast, nirS abundance increases robustly, correlating with Thauera proliferation and enabling functional redundancy that maintains >99% denitrification efficiency despite a 28% reduction in biodiversity. Threshold-dependent behaviors of nosZ and napA genes further reveal that moderate EEF intensities (≤0.050 a.u.) enhance enzymatic activity, while excessive fields cause oxidative damage and metabolic suppression.

These results highlight a dual role for EEF: it enhances chromate degradation through quantum-scale bond destabilization while concurrently modulating microbial functionality. Optimal EEF parameters (≤0.050 a.u.) maximize remediation efficiency by synergizing physical dissociation and biological resilience, whereas higher intensities impair ecosystem stability. This work provides a foundational framework for developing EEF-assisted bioremediation technologies targeting chromium pollution, with future research needed to refine field-scale implementation and hybrid electrochemical-biological integration.

These findings provide practical guidance for the design and optimization of EEF-assisted remediation systems in chromium-contaminated soils and wastewater treatment processes, particularly in identifying optimal electric field intensities that balance degradation efficiency and microbial stability.

However, it should be noted that the DFT simulations were conducted under gas-phase conditions, which may not fully capture solvation effects and complex interactions present in real aqueous environments. Future studies should incorporate solvent models and pilot-scale validation to further enhance the applicability of the proposed approach.

Conflict of Interest: The author(s) declared no potential conflicts of interest with respect to the research, author-ship, and/or publication of this article.

Data Sharing Agreement: The datasets used and/or analyzed during the current study are available from the corresponding author on reasonable request.

Funding: The author(s) received no financial support for the research, authorship, and/or publication of this article.

References

Abdullah, N., N. Yusof, W.J. Lau, J. Jaafar and A.F. Ismail. 2019. Recent trends of heavy metal removal from water/wastewater by membrane technologies. *J. Ind. Eng. Chem*., 76: 17-38.

Anonymous. 2022. Chemical fact sheets: Chromium. *Guidelines Drink-Water Qual.*, 2022: 1-10.

Azimi, A., A. Azari, M. Rezakazemi and M. Ansarpour. 2017. Removal of heavy metals from industrial wastewaters: a review. *Chem. Biol. Eng. Rev*., 4(1): 37-59.

Buckell, M. and D.G. Harvey. 1951. An environmental study of the chromate industry. *Braz. J. Ind. Med*., 8(4): 298.

Cavicchi, R.E. and R.H. Silsbee. 1984. Coulomb suppression of tunneling rate from small metal particles. *Physil. Rev. Lett*., 52(16): 1453.

Cavicchi, R.E. and R.H. Silsbee. 1988. Dynamics of tunneling to and from small metal particles. *Physiol. Rev. Bull*., 37(2): 706.

Che, F., J.T. Gray, S. Ha N. Kruse, S.L. Scott and J.S. McEwen. 2018. Elucidating the roles of electric fields in catalysis: A perspective. *ACS Catal*., 8(6): 5153-5174.

Colussi, I. G. I. N. I. O., A. Cortesi, L.D. Vedova, V. Gallo and F.K.C. Robles. 2009. Start-up procedures and analysis of heavy metals inhibition on methanogenic activity in EGSB reactor. *Bioresour. Technol*., 100(24): 6290-6304.

Dickson, R.M. and A. Becke. 1996. Local density-functional polarizabilities and hyperpolarizabilities at the basis-set limit. *J. Physiol. Chem*., 100(40): 16105-16108.

El Batouti, M., N.F. Al-Harby and M.M. Elewa. 2021. A review on promising membrane technology approaches for heavy metal removal from water and wastewater to solve water crisis. *Water*, 13(22): 3241.

Fan, R., S. Guo, F. Li and X. Zhang. 2017. Dynamics of microbial community and degradation characteristics of mixed organics in a 2-dimensional electric field. *Huanjing Kexue Xuebao*, 37: 3543-3552.

Fu, Y., J. Chi and Y. Wu. 2025. Synergistic electric fields induced by unilateral doping modulation for enhanced organic pollutant degradation and sterilization. *Appl. Surf. Sci.*, 692: 162711.

Gavriş, G., A. Cărăban, O. Stănăşel, G.E. Badea and V. Popa. 2014. Chemical method for treatment wastewaters with chromates. *Fascicula CHIMIE, XXI*, 2014: 27.

Giller, K.E., E. Witter and S.P. McGrath. 1998. Toxicity of heavy metals to microorganisms and microbial processes in agricultural soils: a review. *Soil Biol. Biochem.*, 30(10): 1389-1414.

Huang, Z., X.D. Pan and P.G. Wu. 2013. Health risk assessment of heavy metals in rice to the population in Zhejiang, China. *PLoS One*, 8(9): e75007.

Keldysh, L.V. 1965. Ionization in field of a strong electromagnetic wave. *Sov. Physiol. JETP*, 20(5): 1307-1314.

Kerur, S.S., S. Bandekar, M.S. Hanagadakar, S.S. Nandi, G.M. Ratnamala and P.G. Hegde. 2021. Removal of hexavalent Chromium-Industry treated water and Wastewater: A review. *Mater. Today: Proc*., 42: 1112-1121.

Leyval, C. and E.J. Joner. 2001. Bioavailability of heavy metals in the mycorrhizosphere. *Trace Elem. Rhizosph.*, 2001: 165-185.

Leyval, C., K. Turnau and K. Haselwandter. 1997. Effect of heavy metal pollution on mycorrhizal colonization and function: physiological, ecological and applied aspects. *Mycorrhiza*, 7(3): 139-153.

Li, X., S. Wang, S. Zhao, H. Chang, Y. Li and Y. Zhao. 2023. Effects of an assistive electric field on heavy metal passivation during manure composting. *Sci. Total Environ*., 901: 165909.

Li, Y.W., Y.X. Li and F. Su. 2017. Concentrations and health risk assessment of heavy metals from market rice and vegetables in Pearl Delta river area. *Adv. Environ. Protect*., 7(2): 155-163.

Liu, Z., L. Li and Z. Li. 2018. Removal of sulfate and heavy metals by sulfate-reducing bacteria in an expanded granular sludge bed reactor. *Environ. Technol.*, 39(14): 1814-1822.

Mainier, F.B., P.P.B. Leite and M.F. Reis. 2016. Chromate and the environment: Removal and Utilization of Industrial Waste. *J. Chem*., 10: 147-152.

Miao, Y., R. Liao, X.X. Zhang, Y. Wang, Z. Wang, P. Shi, B. Liu and A. Li. 2015. Metagenomic insights into Cr(VI) effect on microbial communities and functional genes of an expanded granular sludge bed reactor treating high-nitrate wastewater. *Water Res*., 76: 43-52.

Mo, J., Y. Liu, Q. Fu, C. Cai, Y. Lu, W. Wu, Z. Zhao, H. Song, S. Wang and S. Nie. 2022. Triboelectric nanogenerators for enhanced degradation of antibiotics via external electric field. *Nano Energy*, 93: 106842.

Paul, A., S. Dey and D.K. Ram. 2023. Hexavalent chromium pollution and its sustainable management through bioremediation. *Geomicrobiol. J*., 41(4): 324-334.

Prasad, S., K.K. Yadav, S. Kumar and N. Gupta. 2021. Chromium contamination and effect on environmental health and its remediation: A sustainable approaches. *J. Environ. Manag*., 285: 112174.

Qasem, N.A.A., R.H. Mohammed and D.U. Lawal. 2021. Removal of heavy metal ions from wastewater: a comprehensive and critical review. *NPJ Clean Water*, 4(1): 36.

Rodríguez-Chueca, J., A. Mediano, N. Pueyo, I. García-Suescun, R. Mosteo and M. P. Ormad. 2016. Degradation of chloroform by Fenton-like treatment induced by external electric fields: A case of study. *Chem. Eng. Sci*., 156: 89-96.

Seghezzo, L., G. Zeeman, J.B. van Lier and H.V.M. Hamelers and G. Lettinga. 1998. A review: the anaerobic treatment of sewage in UASB and EGSB reactors. *Bioresour. Technol.*, 65(3): 175-190.

Sharma, P., S.P. Singh and S.K. Parakh. 2022. Health hazards of hexavalent chromium (Cr (VI)) and its microbial reduction. *Bioengineered*, 13(3): 4923-4938.

Toriumi, K. and Y. Saito. 1978. Electron-density distribution in crystals of α-K2CrO4. *Acta Crystallogr*. B, 34(11): 3149-3156.

Xiang, H., X. Min, C.J. Tang, M. Sillanpää and F. Zhao. 2022. Recent advances in membrane filtration for heavy metal removal from wastewater: A mini review. *J. Water Process Eng*., 49: 103023.

Yuan, Y. 2014. Research progress in the effect of physical and chemical properties on heavy metal bioavailability in soil-crop system. *Adv. Geosci*., 4(4): 214-223.

Zhang, D., C.Y. Tian and W.X. Mai. 2024a. Exogenous sodium and calcium alleviate drought stress by promoting the succulence of Suaeda salsa. *Plants*, 13(5): 721.

Zhang, X., S. Chen, A.U. Rehman, S. Zhang, Q. Zhang, Y. Liu and S. Li. 2024b. Emerging catalytic strategies driven by external field for heavy metal remediation. *Catalysts*, 14(9): 602.

Zhuang, P., M.B. McBride, H. Xia, N. Li and Z. Li. 2009. Health risk from heavy metals via consumption of food crops in the vicinity of Dabaoshan mine, South China. *Sci. Total Environ*., 407(5): 1551-1561.